

Mode Multiplexing for Scalable Cavity-Enhanced Operations in Neutral-Atom Arrays

Ziv Aqua,^{1,*} Matthew L. Peters,^{1,*} David C. Spierings,¹ Guoqing Wang,^{1,2} Edita Bytyqi,¹ Thomas Propson,¹ and Vladan Vuletić¹

¹*Department of Physics, MIT-Harvard Center for Ultracold Atoms and Research Laboratory of Electronics, Massachusetts Institute of Technology, Cambridge, Massachusetts 02139, USA*

²*International Center for Quantum Materials, School of Physics, Peking University, Beijing 100871, China*

(Dated: November 27, 2025)

Neutral atom arrays provide a versatile platform for quantum information processing. However, in large-scale arrays, efficient photon collection remains a bottleneck for key tasks such as fast, non-destructive qubit readout and remote entanglement distribution. We propose a cavity-based approach that enables fast, parallel operations over many atoms using multiple modes of a single optical cavity. By selectively shifting the relevant atomic transitions, each atom can be coupled to a distinct cavity mode, allowing independent simultaneous processing. We present practical system designs that support cavity-mode multiplexing with up to 50 modes, enabling rapid mid-circuit syndrome extraction and significantly enhancing entanglement distribution rates between remote atom arrays. This approach offers a scalable solution to core challenges in neutral atom arrays, advancing the development of practical quantum technologies.

I. INTRODUCTION

Neutral atom arrays are a leading platform for fault-tolerant quantum computing, offering high-fidelity single- and two-qubit gates [1–6] with arbitrary connectivity enabled by coherent transport of qubits [7, 8]. These capabilities have already supported demonstrations of fault-tolerant logical operations in small quantum error correction (QEC) codes [9, 10]. At the same time, systems with increasingly large array sizes have been realized [11], including recent demonstrations of continuous operation with up to 3000 atoms [12–14]. Despite these advances, utility-level atomic quantum processors are expected to require millions of qubits operating under high-rate QEC cycles [15].

Progress toward this regime can be advanced by improving two essential hardware-level operations: (i) non-destructive qubit readout for mid-circuit measurements (MCM), enabling entropy removal in QEC codes [10, 16–19], and (ii) remote entanglement distribution, enabling scalability through a network of interconnected quantum processing modules [20–27]. Both operations depend on collecting photons scattered by individual atoms in the array. In current systems, this is typically implemented using high numerical-aperture microscope objectives, but their limited collection efficiency ($\lesssim 10\%$) restricts performance. Consequently, non-destructive readout and remote entanglement generation are generally bounded to timescales of several milliseconds [10, 18, 19, 28, 29], introducing a bottleneck for QEC cycle rates and hindering the feasibility of modular scale-up.

Optical cavities provide a promising solution by enhancing atomic emission into a well-defined mode via the Purcell effect [30], enabling both high photon collection efficiencies and strong light–matter interactions

that support fast, cavity-mediated operations. A key figure of merit in this context is the cooperativity, denoted by η , a dimensionless parameter characterizing the strength of the atom–cavity interaction. Recent experiments have demonstrated fast, high-fidelity, non-destructive qubit readout in systems with $\eta > 1$ [31–35], showing that reliable performance is attainable across a wide range of experimental parameters. Additionally, cavity-based schemes have realized atom–photon and remote atom–atom entanglement in both neutral-atom [36–44] and trapped-ion [45–51] systems. Theoretical proposals further suggest that significantly higher entanglement generation rates can be achieved with heralded schemes and improved system parameters [28, 29, 52, 53].

However, integrating optical cavities with large-scale neutral atom arrays presents a significant technical challenge. To date, cavity operations have been restricted to serial execution, with only one atom–cavity interaction occurring at a time. This limitation creates a bottleneck for protocols involving many atoms and hinders scalability to large arrays. Moreover, a fundamental tradeoff arises from the choice of cavity geometry. Since cooperativity scales inversely with the mode area, reducing the cavity mode size generally enhances photon collection efficiency and strengthens atom–photon coupling, enabling faster cavity-mediated operations. On the other hand, tighter mode confinement restricts the number of atoms that can be simultaneously coupled to the cavity mode. As a result, implementations based on small cavities often require transporting atoms into and out of the cavity mode, introducing additional time overhead for large-scale operations. One alternative scaling strategy is to employ multiple cavities, each coupled to an individual atom [54, 55]. While this approach circumvents the single-mode constraints, it typically introduces new challenges, such as restricted optical access and reduced cavity performance. More broadly, an ideal integration approach must preserve the full functionality of neutral-atom arrays. In particular, the performance of two-qubit

* These authors contributed equally to this work.

Rydberg gates in compact cavities can be compromised by stray electric fields arising from charges accumulating on nearby surfaces ($< 100 \mu\text{m}$) [56]. Although mitigation strategies have been explored [57], these remain active areas of research. Collectively, these considerations motivate the need for a scalable cavity integration approach that simultaneously preserves the advantages of high cooperativity, accommodates large atom numbers, keeps the mirror surfaces at sufficient distance from the atoms, and remains generally compatible with the geometrical and other constraints of neutral-atom arrays.

In this work, we introduce a novel approach that enables parallel cavity-enhanced operations on many atoms via multiple modes of a single optical cavity. Interfacing atoms with near-degenerate multimode cavities has previously been explored for various purposes, including tracking the motion of single atoms [58, 59], mediating tunable-range atom-atom interactions [60, 61], realizing Laughlin states of light [62], and enhancing cooperativity [63]. Here, we propose to selectively couple atoms to nondegenerate cavity modes by leveraging local light shifts – building on techniques demonstrated in Ref. [34]. Addressing distinct longitudinal and transverse modes enables both frequency and spatial multiplexing of operations, a concept we term *cavity-mode multiplexing* (CMM). This approach substantially increases operational throughput, alleviating the single-mode tradeoff between cavity size and processing rate. It thus allows the use of larger cavities that are naturally compatible with the geometry of atom arrays and can accommodate many qubits, thereby reducing the need for atom transport. While CMM enables a wide range of applications, in this work we focus on two use cases: (i) rapid syndrome extraction in QEC cycles through parallelized, adaptive qubit measurements, and (ii) fast, fault-tolerant links between logical qubits in distinct modules, achieved via high-rate remote entanglement in a design compatible with intracavity Rydberg gates. For both tasks, when applied to large-scale atom arrays, CMM offers a potential speedup of approximately two orders of magnitude compared to architectures relying on free-space photon collection. Together, these capabilities establish CMM as a promising approach to fast and scalable modular quantum computing with neutral atom arrays.

This paper is organized as follows. In Sec. II, we describe a system overview of CMM with neutral atoms in more detail, including the role of light shifts and mode sorting. We then present two applications of CMM: Sec. III outlines a cavity design tailored for fast syndrome extraction across thousands of qubits, while Sec. IV introduces a different design optimized for high-rate remote entanglement generation and support for teleported CNOT gates between qubits in distant modules. Finally, Sec. V provides concluding remarks and discusses future directions.

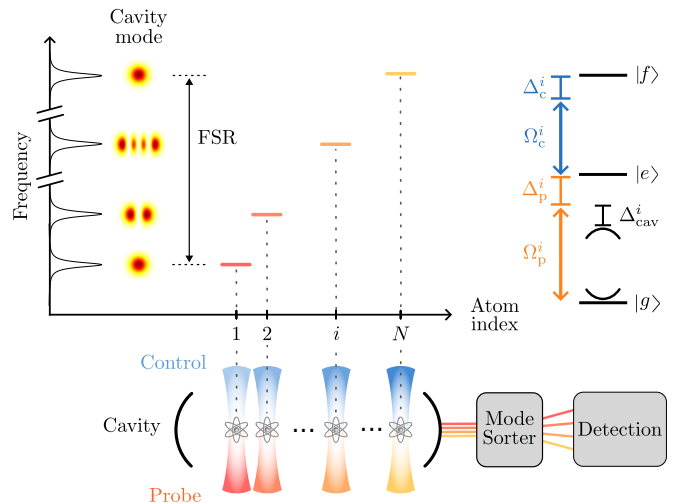


FIG. 1. Conceptual depiction of CMM in an atomic register. The bare cavity spectrum is shown on the left vertical axis, where distinct longitudinal and transverse modes appear at different frequencies. Site-selective control beams (blue) are used to induce light shifts on the excited state $|e\rangle$ via the $|e\rangle \rightarrow |f\rangle$ transition, thereby tuning the $|g\rangle \rightarrow |e\rangle$ transition frequency of each atom to match a different cavity resonance. External probe beams at the corresponding frequencies (red-orange-yellow) excite the atoms, and the emitted photons are coupled into their respective cavity modes. At the cavity output, the different modes are separated by a mode sorter for detection.

II. SYSTEM OVERVIEW

We begin by outlining the physical configuration for implementing CMM with neutral atoms. Consider a register of single atoms trapped in optical tweezers inside a Fabry-Pérot optical cavity, as illustrated in Fig. 1. The cavity supports a rich mode structure comprising both longitudinal and higher-order transverse modes. Longitudinal modes of a fixed transverse profile (e.g., TEM_{00}) are evenly spaced by the free spectral range (FSR) of the cavity. Within each FSR, higher-order transverse modes exhibit distinct resonance frequencies due to their differing spatial profiles and Guoy phase shift [64]. Together, this structure provides a versatile set of spectrally resolved cavity modes that can be harnessed for multiplexing.

The minimal atomic level configuration consists of three states: a ground state $|g\rangle$, an excited state $|e\rangle$, and a higher-lying excited state $|f\rangle$. The cavity mode couples to the $|g\rangle \rightarrow |e\rangle$ atomic transition. To locally control this transition frequency, additional beams addressing each atom couple the excited state $|e\rangle$ to $|f\rangle$ with Rabi frequency Ω_c and detuning Δ_c , inducing a light shift on $|e\rangle$. Since the control beams are far detuned from any ground-state transitions, $|g\rangle$ remains essentially unaffected. Local light shifts induced via excited-to-excited state transitions have been employed in several experimental settings [10, 14, 19, 62, 65–68]. In particular, this technique

has recently been used to selectively decouple atoms from a single cavity mode [34]. With additional polarization control to address specific magnetic sublevels, such shifts have also been proposed as a means to modify cavity-mediated photon–atom gate dynamics [69].

In our setting, the induced shift allows the $|g\rangle \rightarrow |e\rangle$ transition of each atom to be independently coupled near-resonantly to a separate cavity mode, effectively providing each atom with its own dedicated cavity. This configuration supports multiplexed, cavity-enhanced operations across the entire atomic register. As an illustrative example, we consider the case where photons scattered by different atoms are simultaneously collected through separate cavity modes. As depicted in Fig. 1, for each atom i in the register, a probe field drives the shifted transition with Rabi frequency Ω_p^i and detuning Δ_p^i . We denote the detuning of the corresponding cavity mode from the probe frequency by Δ_{cav}^i . Setting $\Delta_{\text{cav}}^i = 0$ ensures maximal photon collection efficiency. In this way, photons scattered by all atoms in the register are simultaneously collected through their assigned cavity modes with high efficiency.

Differentiating the light scattered by each atom requires resolving the corresponding transverse and longitudinal cavity modes. Transverse mode separation can be realized with multi-plane light conversion (MPLC), which performs arbitrary unitary transformations of spatial modes through a sequence of phase masks separated by optical Fourier transform or free-space propagation [70]. This technique has been employed to convert co-located high-order spatial modes into spatially distinct Gaussian beams, scaling to more than a thousand modes [71–73]. The MPLC can be implemented using a programmable spatial light modulator (SLM); however, for static mode sorting, where the required phase remains fixed, custom-fabricated phase masks offer higher spatial resolution at lower optical losses [73, 74]. Longitudinal modes, separated in frequency by the cavity FSR, can be spatially separated using a high-resolving power dispersive element such as a virtually imaged phased array (VIPA) [75, 76], which enables extremely high frequency resolution in excess of $\Delta f/f \sim 10^6$ [77]. Depending on the intended application, the separated modes can then be imaged onto a camera or coupled into single-mode fibers and directed to single-photon detectors for high-efficiency counting.

Achieving multiplexing across many modes while maintaining low crosstalk requires the application of large light shifts to many individual atoms. To keep the required optical powers at practical levels, we consider on-resonance control light ($\Delta_c = 0$) that dresses the states $|e\rangle$ and $|f\rangle$, producing new eigenstates $|e_{\pm}\rangle = (|e\rangle \pm |f\rangle)/\sqrt{2}$. This results in ground-to-dressed-state transitions with frequencies $\mp\Omega_c/2$ relative to the original $|g\rangle \rightarrow |e\rangle$ transition. We constrain the maximum frequency shift, $\Omega_c/2$, such that intensity fluctuations of 0.1% produce frequency variations on the order of the excited-state linewidth Γ , which permits shifts of up

to 2000Γ . The mixing of $|e\rangle$ and $|f\rangle$ also reduces the atom–cavity coupling strengths by a factor of 2, and modifies the dressed-state linewidths compared to the bare state $|e\rangle$. Additionally, we note that beam pointing fluctuations and finite atomic temperature can lead to heating from dipole force fluctuations due to the large \sim GHz potential depth differences between ground states and excited dressed state $|e_{+}\rangle$, which we assume is well-controlled. It is important to note that, while the following discussion focuses on implementing CMM with ^{87}Rb atoms, the concepts presented are readily applicable to other alkali and alkaline–earth species, as well as to ions.

III. SYNDROME EXTRACTION

Error-corrected quantum computing relies on MCM of syndrome qubits to identify and correct errors occurring in the data qubits encoding the logical quantum information. In neutral-atom arrays, syndrome extraction via free-space imaging typically requires several milliseconds, constituting a substantial fraction of the QEC cycle duration. Optical cavities, in contrast, enable non-destructive qubit readout on the microsecond timescale by coupling one of the qubit states, $|1\rangle$, to an excited state, $|e\rangle$, via the cavity mode, as illustrated in Fig. 2(a). Common techniques include fluorescence detection, where probe light addressing the $|1\rangle \rightarrow |e\rangle$ transition is applied via an external beam and the scattered photons are collected through the cavity [31, 33, 34]; and transmission detection, where the presence of an atom in $|1\rangle$ suppresses resonant cavity transmission [32, 33, 35, 78]. However, even with microsecond-scale qubit readout, sequentially measuring thousands of syndrome qubits extends the total duration to the millisecond range. In this regime, the added complexity of integrating a cavity offers limited benefit compared to parallel free-space imaging, which can simultaneously read out large qubit arrays.

For syndrome extraction, the ability to couple multiple qubits simultaneously to the same cavity mode provides a significant advantage, enabling more efficient readout strategies than sequential readout [34]. In practical quantum computers, the physical qubit error rates are expected to be small. This implies that the vast majority of syndrome qubits will occupy the $|0\rangle$ state (indicating the absence of an error) while only a small fraction will be in the $|1\rangle$ state (signifying the presence of an error). This inherent bias can be exploited to perform global checks: rather than measuring each syndrome qubit individually, one can probe an entire batch of n_{batch} atoms simultaneously to determine whether any are in $|1\rangle$. If no error is detected—an outcome that is likely given the low error probability—the procedure advances directly to the next batch. If an error is detected, an adaptive binary search can be performed by selectively decoupling subsets of atoms from the cavity mode through locally controlled light shifts, enabling efficient identification of the faulty syndrome qubit(s). In cases where multiple

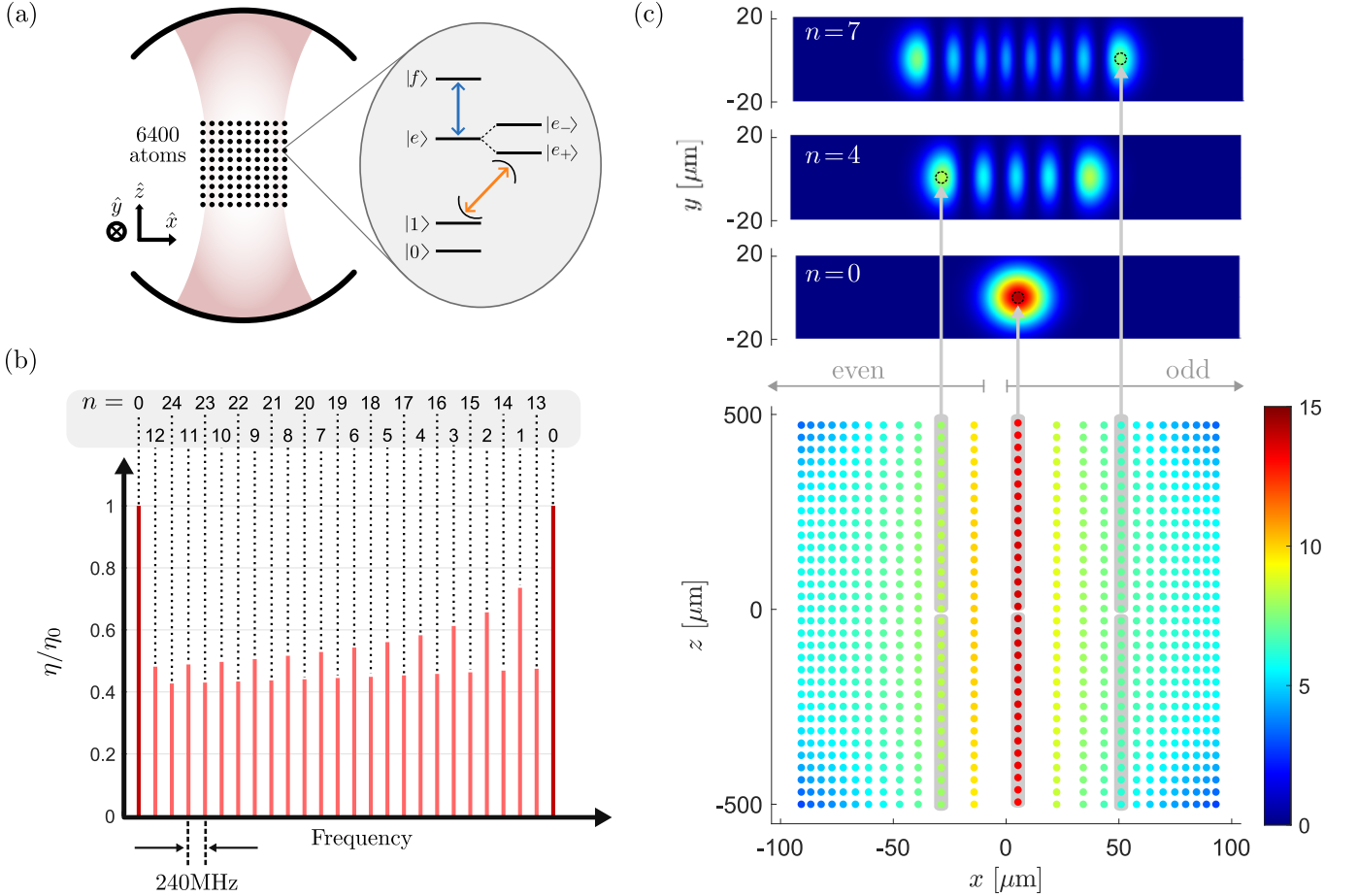


FIG. 2. Cavity and atom-array configuration for syndrome readout using CMM with $\text{HG}_{n,0}$ modes. (a) Left: atom array with up to 6400 atoms, each coupled to a cavity mode. Right: atomic level scheme used for qubit readout. (b) Cavity spectrum showing the peak cooperativity of 25 equally-spaced HG modes spanning the FSR. Cooperativity values are normalized to η_0 , the peak cooperativity of the $\text{HG}_{0,0}$ mode. (c) Top: Spatial profiles of $\text{HG}_{n,0}$ modes with indices $n = 0, 4, 7$. Bottom: Cooperativity per atom across the array (every 8th atom shown). The color bar indicates cooperativity in both the mode profiles and the atom array map. Columns of atoms are placed at the intensity maxima of the $\text{HG}_{n,0}$ modes as indicated by the dashed circles, with odd (even) values of n assigned to the positive (negative) x -axis. Each column is divided into two registers, which couple to two longitudinal cavity modes with the same transverse profile, separated in frequency by one FSR.

erroneous syndromes are present within the same batch, the global check and binary search sequence are repeated until all errors are located. For an independent probability of a faulty syndrome p_{synd} , the expected number of queries m required per batch is,

$$m = 1 + n_{\text{batch}} p_{\text{synd}} [1 + \log_2 (n_{\text{batch}})], \quad (1)$$

where the first term corresponds to the single global check that is always performed. The second term accounts for the additional queries required when faulty syndromes are present: each faulty syndrome triggers a binary search, followed by a global check to confirm that no further faulty syndromes remain within the batch. This process requires $1 + \log_2(n_{\text{batch}})$ queries per faulty syndrome, and is multiplied by the expected number of faulty syndromes per batch, $n_{\text{batch}} p_{\text{synd}}$.

With a single cavity mode, the expected number of

steps required to process N syndrome qubits is

$$\# \text{ steps} = \left\lceil \frac{N}{n_{\text{batch}}} \right\rceil \times m, \quad (2)$$

where $\lceil N/n_{\text{batch}} \rceil$ is the number of batches that must be processed sequentially. For $p_{\text{synd}} = 5 \times 10^{-3}$, a maximum batch size of $n_{\text{batch}} = 256$, and a query time of $10 \mu\text{s}$, the total readout duration enters the millisecond regime when $N \approx 2000$ atoms, not accounting for additional time overhead from transporting atom batches in and out of the cavity. Therefore, even with adaptive searches, a single cavity mode does not provide a net advantage over parallel free-space imaging. If, however, adaptive searches can be performed in parallel across multiple registers—each coupled to a distinct cavity mode—the scal-

ing improves to,

$$\# \text{ steps} = \lceil \frac{N}{n_{\text{batch}} n_{\text{modes}}} \rceil \times m, \quad (3)$$

where n_{modes} denotes the number of available modes.

To realize this parallelism using CMM, we propose the following design, tailored to ^{87}Rb atoms. We define the relevant atomic states as

$$\begin{aligned} |0\rangle &\equiv |5S_{1/2}, F = 1, m_F = 1\rangle, \\ |1\rangle &\equiv |5S_{1/2}, F = 2, m_F = 2\rangle, \\ |e\rangle &\equiv |5P_{3/2}, F' = 3, m_F = 3\rangle, \\ |f\rangle &\equiv |4D_{5/2}, F'' = 4, m_F = 4\rangle. \end{aligned} \quad (4)$$

These qubit states are employed solely during readout; the qubit need not remain encoded in these states throughout computation. Since the measurement projects the qubit into either $|0\rangle$ or $|1\rangle$, coherence preservation is not required at this stage, which simplifies changing the basis from the computational encoding—typically the clock states with $m_F = 0$ —to the readout encoding. It is important to note that the use of the cycling transition for $|e\rangle \rightarrow |f\rangle$ prevents mixing with other states that could induce readout errors via depumping channels from $|1\rangle$ to $|0\rangle$ or out of the logical subspace.

For this atomic configuration, we consider a Fabry-Pérot optical cavity characterized by the parameters summarized in Table I. We tune the cavity such that the higher-order Hermite-Gauss modes along the transverse x-axis, $\text{HG}_{n,0}$ with $n \in [0, 24]$, are arranged to be equally spaced in frequency within the FSR, with a 240 MHz separation between adjacent modes. Using these HG modes across two FSRs provides access to a total of 50 equally spaced cavity modes (see Fig. 2(b)). The control beams, resonant with the $|e\rangle \rightarrow |f\rangle$ transition, are used to dress the excited states, allowing to tune the $|1\rangle \rightarrow |e_+\rangle$ transition of each atom to couple to the appropriate cavity mode. The total frequency range spans 12 GHz, and with 0.1% intensity stability of the control field, the resulting variation of the ground-to-dressed-state transition frequency is limited to the linewidth of $|e\rangle$, $\Gamma/2\pi = 6$ MHz.

TABLE I. Parameters of the optical cavity used for syndrome extraction.

Cavity length	25 mm
Mode waist	20 μm
Rayleigh range	1.6 mm
Finesse	6×10^4
FSR	6 GHz
Linewidth (FWHM)	100 kHz

In addition to parallelized syndrome extraction, this architecture increases the number of atoms that can be accommodated within the cavity. Rather than being restricted to the spatial extent of the fundamental Hermite-

Gaussian (HG_{00}) mode, columns of atoms are arranged along the z -axis at the intensity maxima of each higher-order HG mode, positioned at different points along the x -axis (Fig. 2(c)). To reduce crosstalk and increase the spatial separation between adjacent columns of atoms, we assign modes with odd (even) n to the positive (negative) x -axis, taking advantage of the symmetry of the intensity peaks about the y -axis. With a minimum spacing of about 4 μm between adjacent atoms, this arrangement allows up to 6400 atoms to couple to some mode of the cavity at once, enabling simultaneous operations on 50 distinct batches of 128 atoms each.

Figure 2(d) shows the cooperativity η per atom for the $|1\rangle \rightarrow |e_+\rangle$ transition, accounting for (i) the reduction in atom-cavity coupling and decay rate due to the dressed-state nature of $|e_+\rangle$, (ii) the Gaussian mode Rayleigh range, which reduces coupling for atoms farther from the cavity center along z , and (iii) the electric field profile of higher-order modes, which results in lower atom-cavity coupling as n increases. The resulting average cooperativity is $\bar{\eta} = 6.8$, with a standard deviation of $\sigma_\eta = 1.9$ across the array. This configuration enables fast, high-fidelity fluorescence readout. The atoms are individually addressed by probe beams with Rabi frequency $\Omega_p/(2\pi) = 15$ MHz and detuning $\Delta_p/(2\pi) = 120$ MHz relative to the dressed transition of each atom, while the corresponding cavity mode is kept on resonance with the probe field ($\Delta_{\text{cav}} = 0$). Under these conditions, each atom in state $|1\rangle$ scatters ~ 20 photons into the cavity mode within 10 μs at a collection efficiency exceeding 80%. The combination of individual probe addressing and frequency separation between cavity modes suppresses crosstalk to below 10^{-5} . Additionally, assuming $p_{\text{synd}} = 5 \times 10^{-3}$, the dispersive frequency shift of a given cavity mode due to the presence of faulty syndrome qubits in other modes is smaller than 10% of the cavity linewidth, leading to less than a 10% decrease in the collection efficiency. Furthermore, the frequency stability of the dressed state ensures that readout times vary by less than 10%, as the frequency fluctuations are small compared to the probe detuning Δ_p . Alternatively, other readout techniques could be employed to achieve comparable or improved performance by coupling light into the different cavity modes via the mode sorter; however, a detailed description of such methods lies beyond the scope of this work.

With 50 available modes and a query time of 10 μs , this design yields a substantial improvement in syndrome extraction speed. Following Eqs. 1–3, Fig. 3 compares the scaling of syndrome readout duration with the number of atoms for three cases: a 5 ms free-space readout; adaptive searches utilizing a single cavity mode; and adaptive searches employing 50 cavity modes. As discussed above, a single-mode system reaches the millisecond timescale at approximately 2000 atoms. However, CMM with 50 modes in the proposed design achieves an improvement of more than two orders of magnitude over free-space imaging, completing syndrome extraction in 50 μs for 5000

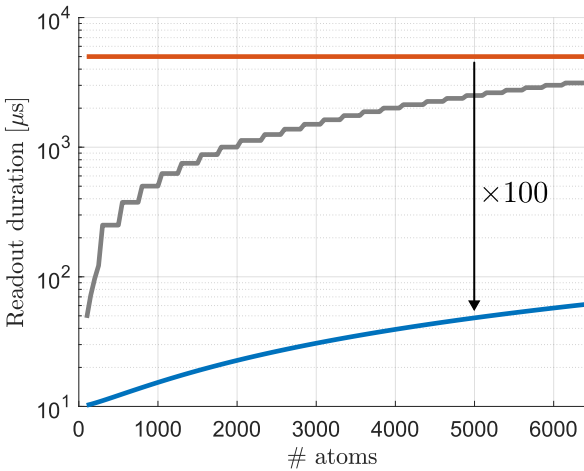


FIG. 3. Scaling of syndrome readout duration using free-space imaging (orange), a single cavity mode (grey), and CMM over 50 cavity modes (blue), assuming $p_{\text{synd}} = 5 \times 10^{-3}$ and 10 μs query time. Compared to free-space readout, CMM offers a speed-up of two orders of magnitude, allowing readout of 5000 syndrome qubits within 50 μs .

atoms. Beyond this speedup, cavity readout also strongly suppresses decoherence of the data qubits from stray photon scattering: in free-space imaging a large fraction of photons are emitted into uncontrolled directions, including toward the data qubits, whereas in the cavity configuration over 80% of the photons are collected into the cavity modes, thereby strongly reducing this effect. Moreover, the cavity-enhanced photon collection efficiency allows fewer photons to be scattered during readout, which minimizes heating and ensures that the measured atoms can be readily reused for subsequent operations.

Our scheme is compatible with a zoned architecture for neutral atom arrays. Entanglement via Rydberg gates can be performed within the cavity, and the readout zone described in this design spans only 200 μm along the x -axis. This zone can be further restricted to a subset of the available sites while still maintaining an average cooperativity of $\bar{\eta} > 6$. Additionally, we note that to fully exploit the benefits of adaptive search, individual control over the light dressing beams in two dimensions is required, a capability actively pursued by several research efforts [79–85]. In the following application involving a one-dimensional array, this level of control is readily available using acousto-optic deflectors (AODs).

IV. MODULAR CONNECTIVITY

As atom array sizes advance into the regime of thousands of qubits [11, 14], further scaling is expected to encounter significant technical challenges, including the demand for higher laser powers, the requirement for large microscope field of view with high spatial resolution, and

the difficulty of maintaining beam uniformity over large areas. Current estimates for utility-scale quantum computation indicate that millions of qubits will be required to implement practical, fault-tolerant algorithms [15, 86–89]. A promising route toward achieving this scale is a modular architecture, in which fixed-size atom array nodes are interconnected via optical links, thereby enabling distributed quantum computation. With an appropriately designed light–matter interface, such a modular scheme can, in principle, be scaled to arbitrarily large system sizes. Beyond scalability, a key advantage of this approach lies in its flexibility: it allows the array size within each module to be tailored for optimal operational performance—such as achieving high-fidelity gates—while avoiding the physical constraints associated with very large monolithic arrays.

At the heart of such a modular design lies the ability to generate remote entanglement between nodes. Bell pairs shared across different modules, together with local operations at each node, provide the necessary building blocks to implement inter-module operations [27, 44, 90]. As a concrete example, we consider the implementation of teleported CNOT gates [91] between qubits located in different nodes, which can be used to fault-tolerantly connect logical qubits encoded in surface codes across separate modules [26]. The protocol begins with the distribution of a remote Bell state between two *communication qubits*. Each communication qubit is then entangled with a corresponding *code qubit* at the same node via a local CNOT gate. The communication qubits are subsequently measured, and the outcomes are classically communicated to determine the appropriate single-qubit rotations to apply to the code qubits. This sequence of operations results in the realization of a teleported CNOT gate between the remote code qubits. Overall, the procedure combines several essential capabilities: remote Bell state generation, local single- and two-qubit gates, and qubit readout. Achieving a high QEC cycle rate requires that all these operations be executed on a short timescale.

There are several approaches for generating a Bell state between two remote atomic qubits [41, 53, 92, 93]. Here, we focus on a scheme in which atom–photon entanglement is first prepared independently at each node by emitting a single photon from each communication atom. Photons from different nodes—each entangled with its local qubit—are then routed to a probabilistic Bell-state measurement (BSM), which heralds the creation of an atom–atom Bell state [94–97]. The main benefit of this scheme lies in its heralding property: only successful events are retained, ensuring that subsequent operations are performed on a known entangled state. However, since the BSM relies on detection of both photons, the overall success probability for generating atom–atom entanglement scales quadratically with the photon collection efficiency,

$$P_s = \frac{1}{2} (\alpha_{\text{interface}} \times \alpha_{\text{setup}})^2, \quad (5)$$

where the factor of 1/2 reflects the intrinsic success probability of the BSM, $\alpha_{\text{interface}}$ denotes the probability of obtaining a photon at the cavity output, and α_{setup} accounts for the efficiency of the optical setup, including fiber coupling, all optical elements in the path, and detection efficiency.

In free-space implementations, high-numerical-aperture lenses are used to collect the emitted photons, but their limited collection efficiency restricts Bell pair generation rates to about 250 Hz [28, 96, 97]. A notable advantage of the free-space approach is its ability to attempt entanglement generation in parallel across many communication qubits, leading to a linear scaling of the total rate with the number of available qubits. For example, with roughly 4000 communication atoms, rates approaching the MHz regime could be achieved, albeit at the cost of dedicating a considerable fraction of the total array to communication rather than computation. However, even at these high entangling rates, inter-module operations would remain limited by the qubit readout duration, typically on the order of a few milliseconds.

Optical cavities provide an efficient atom–photon interface, significantly improving photon collection and enabling higher Bell pair generation rates. Arrays of microcavities have been proposed as a path towards generation rates in the tens of MHz, with estimates for individual microcavities reaching up to 2.4 MHz [29]. Within a single cavity mode, Bell-state generation attempts must be performed sequentially, and in small-mode-volume cavities, which can accommodate only a few atoms, the attempt rate is limited by the speed of atom transport through the cavity. Additionally, in such compact architectures, local operations can further limit the rate of teleported CNOT gates. Qubit readout could be performed either via free-space imaging, which is inherently slow, or via cavity-based measurement, which requires transporting all communication qubits that successfully generated Bell pairs back into the cavity, introducing substantial time overheads. Moreover, for microcavities, executing two-qubit Rydberg gates would likely require atom transport to a suitable distance away from the cavity structure, adding further complexity to the implementation. We note that relying on atom transport not only slows inter-module operations but also requires additional measures to preserve coherence, such as dynamical decoupling pulse sequences [8]. A distinct path is offered by a cavity-array microscope architecture in which each communication atom couples to its own cavity [55]. By supporting long working distances that preserve high-fidelity intra-cavity Rydberg interactions, this design minimizes atom motion and enables parallelization that can more than compensate for the lower per-cavity entanglement rates compared to microcavities.

We propose an alternative approach based on CMM, which enables parallel Bell-state generation attempts within a single-cavity design that can host many qubits and remains compatible with intra-cavity Rydberg gates,

thereby reducing the reliance on atomic motion. To illustrate this concept, we present a system design tailored to ^{87}Rb that implements atom–photon entanglement generation via vacuum-stimulated Raman adiabatic passage (vSTIRAP), following the method demonstrated in [36, 98]. The relevant atomic states, shown in Fig. 4(a), are defined as

$$\begin{aligned} |0\rangle &\equiv |5S_{1/2}, F=1, m_F=-1\rangle, \\ |1\rangle &\equiv |5S_{1/2}, F=1, m_F=1\rangle, \\ |g\rangle &\equiv |5S_{1/2}, F=2, m_F=0\rangle, \\ |e\rangle &\equiv |5P_{3/2}, F'=1, m_F=0\rangle, \\ |f\rangle &\equiv |4D_{5/2}, F''=2, m_F=0\rangle. \end{aligned} \quad (6)$$

The atom–photon entanglement protocol proceeds as follows. The atom is first initialized in $|g\rangle$. An external field then drives the $|g\rangle \rightarrow |e_+\rangle$ transition, inducing a vSTIRAP process that generates a single photon in the cavity whose polarization (σ^+ or σ^-) is entangled with the atomic qubit state:

$$|\psi_{\text{final}}\rangle = \frac{1}{\sqrt{2}}(|0, \sigma^+\rangle + |1, \sigma^-\rangle). \quad (7)$$

In this scheme, the probability of obtaining a photon at the cavity output is given by

$$\alpha_{\text{interface}} = \frac{\eta}{\eta+1} \times \frac{\kappa_e}{\kappa_e + \kappa_i}, \quad (8)$$

where κ_e is the cavity decay rate into the designated output mode and κ_i is the decay rate associated with intrinsic cavity losses. An important feature of this scheme is that the external drive can be used to shape the temporal wavefunction of the emitted photon [99]. Such control over the photon envelope is essential for ensuring the indistinguishability of photons generated across different modules, thereby enabling high-fidelity BSMs even in the presence of variations in system parameters between modules.

We consider a Fabry–Pérot cavity characterized by the parameters summarized in Table II. The total cavity linewidth consists of the coupling rate to the output mode, $\kappa_e/(2\pi) = 2.3\text{ MHz}$, and the internal loss rate, $\kappa_i/(2\pi) = 38\text{ kHz}$, assuming mirror losses of 10 ppm. In contrast to the case of syndrome extraction, simultaneously coupling multiple atoms to the same cavity mode offers no advantage for atom–photon entanglement. We therefore employ higher-order radial Laguerre–Gauss modes, $\text{LG}_{p,0}$ with $p \in [0, 32]$. As depicted in Fig. 4(c), the peak intensity of these modes at $(x, y) = (0, 0)$ remains constant with p , ensuring a mode-independent atom–cavity coupling at that location. The cavity is tuned so that these modes are equally spaced in frequency across the FSR, with 727 MHz separation between adjacent modes. Similarly to the syndrome extraction case, control beams resonant with the $|e\rangle \rightarrow |f\rangle$ transition dress the excited states, enabling the $|0\rangle \rightarrow |e_+\rangle$ and

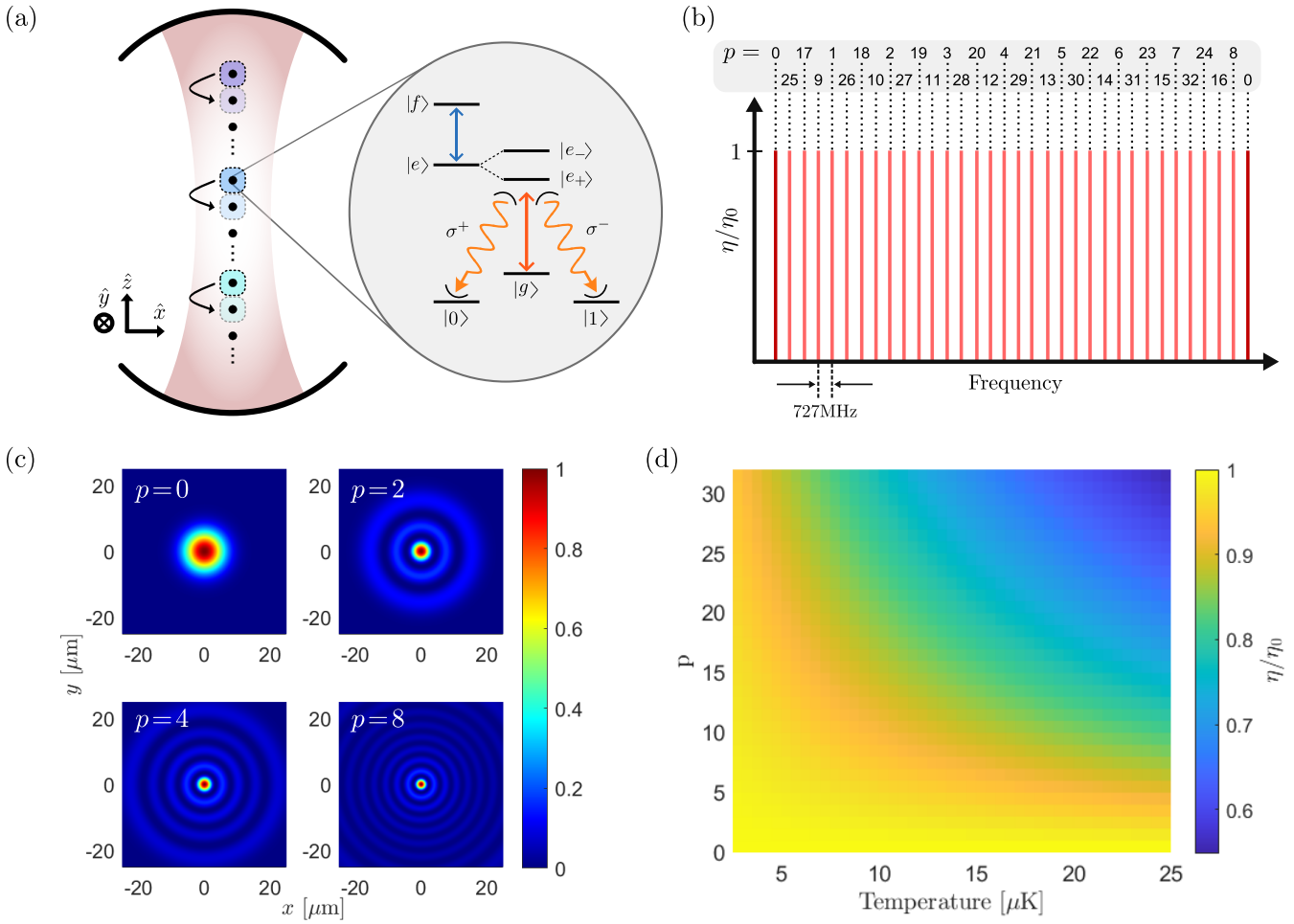


FIG. 4. Cavity and atom-array configuration for remote atom-atom Bell-state generation using CMM with radial $\text{LG}_{p,0}$ modes. (a) Left: 1D array with up to 255 atoms, where each atom is coupled to one of the cavity modes. Groups of consecutive atoms form registers, each associated with a distinct cavity mode. A control beam scans across the array, sequentially coupling atoms in each register to their assigned mode. Right: atomic level scheme for atom-photon entanglement via vSTIRAP. (b) Cavity spectrum showing the peak cooperativity of 33 equally-spaced LG modes across the FSR, given relative to the peak cooperativity of the $\text{LG}_{0,0}$ mode, denoted η_0 . The peak cooperativity remains unchanged for the higher-order radial LG modes. (c) Spatial profiles of $\text{LG}_{p,0}$ modes with indices $p = 0, 2, 4, 8$. (d) Cooperativity reduction of each mode as a function of temperature.

$|1\rangle \rightarrow |e_+\rangle$ transitions to be tuned into resonance with the desired cavity mode. A maximum frequency shift of 12 GHz with 0.1% intensity stability keeps fluctuations of the dressed-state transition within the natural linewidth, $\Gamma/2\pi = 6$ MHz. While this tuning range does not span the full FSR, it provides access to 17 cavity modes.

TABLE II. Parameters of the optical cavity used for modular connectivity.

Cavity length	6.25 mm
Mode waist	8.6 μm
Rayleigh range	0.3 mm
Finesse	10^4
FSR	24 GHz
Linewidth (FWHM)	2.34 MHz

We arrange 225 atoms in a one-dimensional array along the z -axis with a spacing of approximately 3 μm , such that the outermost atoms lie roughly one Rayleigh length from the cavity center. Individual atoms are addressed by control beams focused to a 2 μm waist. At this tight spacing, however, residual light shifts on neighboring atoms are unavoidable, compromising the selective addressing of individual atoms. For the maximum applied frequency shift of 12 GHz, adjacent atoms experience residual shifts of approximately 1 GHz. To mitigate the crosstalk between control beams, the array is divided into registers of consecutive atoms, with each register associated with a single cavity mode. Within each register, the control beam is scanned sequentially to couple individual atoms to the appropriate mode for atom-photon entanglement. This procedure is performed in parallel across all regis-

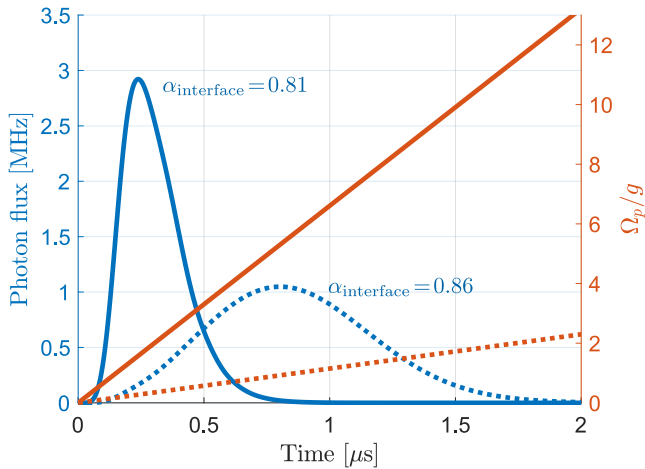


FIG. 5. Photon generation using vSTIRAP. Simulated photon flux at the cavity output (blue) produced by a linearly increasing external probe field (orange) as a function of time. The simulation assumes $\eta=7$ and the cavity parameters described in the main text. The solid and dotted lines correspond to two different slopes of the external probe, resulting in distinct photon temporal profiles, with the solid line representing the probe drive chosen for our application. The dotted probe drive saturates the vSTIRAP adiabaticity condition, resulting in the photon generation probability given by Eq. 8, but at the cost of a reduced generation rate.

ters, as illustrated in Fig. 4(a). By increasing the spacing between simultaneously active control beams, this scheme substantially suppresses the crosstalk between the beams. Nevertheless, neighboring atoms can still experience residual light shifts that may couple them to cavity modes outside their assigned register. To prevent such unintended interactions, cavity modes with resonance frequencies within the range of the maximum residual shift are excluded from use. In practice, this constraint eliminates the two lowest-frequency modes, while the next available mode remains sufficiently detuned to suppress unwanted coupling. Consequently, a total of 15 cavity modes are available, enabling the 225-atom array to be partitioned into 15 registers of 15 atoms each.

This configuration yields an average cooperativity of $\bar{\eta}=7$, with a standard deviation of $\sigma_\eta=1.8$ across the array. In the calculation, we account for the branching ratios of $|e_+\rangle$ to the atomic qubit states, the variation of atom–cavity coupling along the z -axis, and an assumed atomic temperature of $10\,\mu\text{K}$. The latter plays an important role for higher-order LG modes, where the central lobe narrows with increasing p . Consequently, the finite spatial extent of the atomic wavefunction reduces the effective atom–cavity coupling, as illustrated in Fig. 4(d).

With this cooperativity, it is possible to implement vSTIRAP using an external probe field resonant with the $|g\rangle \leftrightarrow |e_+\rangle$ transition and a cavity mode tuned to the $|0,1\rangle \leftrightarrow |e_+\rangle$ transition. Using Eqs. 5 and 8, and assuming an optical setup efficiency of $\alpha_{\text{setup}}=0.75$, the

predicted atom–atom entanglement success probability is $P_s=0.21$. This value corresponds to the ideal case where the vSTIRAP adiabaticity condition is fully saturated and η is uniform across the array. To assess the performance under realistic conditions, we simulate the process for the entire 225-atom array, including all relevant atomic levels, using a linearly increasing drive. As shown in Fig. 5, the external probe allows control over the temporal profile of the output photon. This reveals a trade-off between photon generation probability—maximized when the adiabaticity condition is saturated—and the achievable generation rate. Balancing these factors, our chosen parameters yield an average success probability of $\bar{P}_s=0.18$ across the array. With CMM over the 15 modes, the corresponding atom–atom Bell-state generation rate is 4 MHz. We note that the system parameters and drive profile can be further optimized to increase this rate, however, such optimization lies beyond the scope of this work.

The protocol remains robust against transition frequency fluctuations, where a 6 MHz atomic detuning leads to less than a 1% change in the atom–atom Bell-state probability. This robustness allows operation in a magnetic field, which induces Zeeman shifts to the $|0\rangle$ and $|1\rangle$ qubit states, and is essential for implementing high-fidelity Rydberg gates. Additional imperfections arise from spontaneous decay out of $|f\rangle$ into other states in the $5P_{3/2}$ manifold. Most such decay channels only reduce the photon collection efficiency, but decay to the $|F'=1, m_F=\pm 1\rangle$ states can also produce a photon in the cavity while leaving the atom in $|F=1, m_F=0\rangle$. This occurs with a probability of less than 1%, and can be mitigated using a measurement that discriminates between the magnetic sublevels of the $F=1$ manifold. We further emphasize that, although the $|e\rangle \leftrightarrow |f\rangle$ transition is not a cycling transition, a π -polarized control beam prevents any unwanted mixing with other states. This is because the π -polarized transitions from $|e\rangle$ to $|F''=1, 3, 4, m_F=0\rangle$ are forbidden; the transition to $|F''=1, m_F=0\rangle$ is excluded by the $\Delta F=0, \Delta m_F=0$ selection rule, while transitions to $|F''=3, 4\rangle$ are forbidden since they require $\Delta F>1$. Under these conditions, the achievable atom–atom Bell-state fidelity is sufficient for modular architectures, since the threshold for stitching surface-code patches across modules can be as high as 10% [26].

To evaluate the implications for fault-tolerant architectures, we connect our results to the cycle time of a distance-20 surface code, which requires on the order of 40 teleported CNOT gates per cycle between distant code patches. In our construction, the communication atoms remain fixed in place throughout the entire process, ensuring stable coupling and minimizing the use of atom transport. The sequence of operations proceeds as follows. First, the communication qubits are initialized in $|g\rangle$; we assume that state preparation, together with occasional recoiling, requires 16 μs per cycle [28]. Next, since the expected number of successful

pairs equals the number of atoms times P_s , the 40 required Bell pairs shared between modules can be generated in a single multiplexed scan across the array. With a control-beam switching time of 100 ns, the scan completes within 12 μ s. In the following step, Rydberg gates are performed between the successful communication qubits and the code qubits. This process involves qubit basis changes, transporting the code qubits, and the Rydberg interactions themselves. The dominant contribution here is the atomic motion, as Raman manipulations and Rydberg gates operate in the MHz regime [9]. Because Rydberg operations can be carried out directly within the cavity, the surface code patch can be positioned near the cavity mode, allowing short-range transport. We estimate this step at approximately 20 μ s. Finally, measurement of the 40 communication qubits is performed. With a 10 μ s measurement time multiplexed over 15 modes, this requires roughly 25 μ s. Adding these contributions, the full sequence of 40 teleported CNOTs completes in about 70 μ s. This cycle time is roughly two orders of magnitude faster than free-space implementations, while requiring significantly fewer communication qubits.

V. DISCUSSION

We have introduced mode-multiplexed optical cavities as a scalable interface for neutral atom arrays. In our approach, atoms are selectively coupled to multiple modes of a single cavity using light shifts induced via an excited-to-excited atomic transition. This enables parallel cavity-enhanced operations, allowing fast processing in cavities large enough to accommodate large-scale atom arrays. As a result, the need for atom transport in and out of the cavity is minimized and the configuration maintains full compatibility with existing capabilities of the neutral atom platform.

We presented two applications of CMM in the context of quantum computing. First, for MCM of syndrome qubits, our approach reduces the readout duration by two orders of magnitude compared to free-space readout for systems with thousands of qubits. The scheme combines two key capabilities: the ability to couple many atoms to the same mode, which allows an adaptive search for faulty syndrome qubits, and the ability to perform this search in parallel across multiple cavity modes. Beyond the favorable logarithmic scaling of binary search, adaptive syndrome extraction has also been proposed as a strategy to enhance code performance and shorten QEC cycles by prioritizing specific syndrome sets in time [100],

a capability that our scheme naturally supports. Second, we highlight the advantages of CMM in a modular atom array architecture. In this setting, the mode-multiplexed interface supports fast inter-module operations by enabling high-rate remote entanglement of atomic qubits, and fast local operations such as cavity-based readout and intracavity Rydberg gates. Together, these capabilities provide fast, fault-tolerant connectivity between logical qubits encoded in distant modules, supporting distributed quantum computing with neutral atom arrays.

To fully realize the benefits of CMM, several challenging hardware requirements must be addressed. One key aspect is precise control over the cavity symmetry: either maintaining cylindrical symmetry to support LG modes or intentionally breaking it to produce HG modes in the desired orientation. Such control can be achieved by mounting one of the cavity mirrors on a 3D piezo translation stage, as demonstrated in Ref. [101]. Another crucial requirement is the ability to individually address atoms, enabling the application of local light shifts and the probing of atoms at distinct frequencies corresponding to their shifted transitions. This capability is being actively explored, and both experiments and theoretical proposals point toward feasible implementations [79–85].

We note that, in addition to Fabry–Pérot cavities, this approach can be implemented in other cavity geometries. For instance, bow-tie cavities allow for small mode waists while supporting longer cavity lengths, enabling high-cooperativity designs with smaller FSRs. This configuration reduces reliance on high-order spatial modes, instead making greater use of longitudinal modes of lower-order transverse profiles. In the context of remote entanglement, this can help maintain a high average cooperativity at elevated atomic temperatures, thereby reducing the amount of required atom cooling.

ACKNOWLEDGMENTS

We thank Ohad Lib and Nicolas Fontaine for useful discussions on spatial mode sorting. This work is supported by a collaboration between the US DOE and other Agencies. This material is based upon work supported by the U.S. Department of Energy, Office of Science, National Quantum Information Science Research Centers, Quantum Systems Accelerator. We acknowledge support from the MIT-Harvard Center for Ultracold Atoms (an NSF Frontier Center, award # PHY-2317134), the NSF Quantum Leap Challenge Institute (award # 2016244), and the NSF-funded QuSeC-TAQS program (award # 2326787).

[1] H. Levine, D. Bluvstein, A. Keesling, T. T. Wang, S. Ebadi, G. Semeghini, A. Omran, M. Greiner, V. Vuletić, and M. D. Lukin, Dispersive optical systems for scalable Raman driving of hyperfine qubits, *Phys. Rev. A* **105**, 032618 (2022).

[2] S. J. Evered, D. Bluvstein, M. Kalinowski, S. Ebadi, T. Manovitz, H. Zhou, S. H. Li, A. A. Geim, T. T. Wang, N. Maskara, H. Levine, G. Semeghini,

M. Greiner, V. Vuletić, and M. D. Lukin, High-fidelity parallel entangling gates on a neutral-atom quantum computer, *Nature* **622**, 268 (2023).

[3] R. B.-S. Tsai, X. Sun, A. L. Shaw, R. Finkelstein, and M. Endres, Benchmarking and Fidelity Response Theory of High-Fidelity Rydberg Entangling Gates, *PRX Quantum* **6**, 010331 (2025).

[4] A. Radnaev, W. Chung, D. Cole, D. Mason, T. Balance, M. Bedalov, D. Belknap, M. Berman, M. Blakely, I. Bloomfield, P. Buttler, C. Campbell, A. Chopinaud, E. Copenhaver, M. Dawes, S. Eubanks, A. Friss, D. Garcia, J. Gilbert, M. Gillette, P. Goiporia, P. Gokhale, J. Goldwin, D. Goodwin, T. Graham, C. Guttormsson, G. Hickman, L. Hurtley, M. Iliev, E. Jones, R. Jones, K. Kuper, T. Lewis, M. Lichtman, F. Majde-teimouri, J. Mason, J. McMaster, J. Miles, P. Mitchell, J. Murphree, N. Neff-Mallon, T. Oh, V. Omole, C. Parlo Simon, N. Pederson, M. Perlin, A. Reiter, R. Rines, P. Romlow, A. Scott, D. Stiefvater, J. Tanner, A. Tucker, I. Vinogradov, M. Warter, M. Yeo, M. Saffman, and T. Noel, Universal Neutral-Atom Quantum Computer with Individual Optical Addressing and Nondestructive Readout, *PRX Quantum* **6**, 030334 (2025).

[5] M. Peper, Y. Li, D. Y. Knapp, M. Bileska, S. Ma, G. Liu, P. Peng, B. Zhang, S. P. Horvath, A. P. Burgers, and J. D. Thompson, Spectroscopy and Modeling of Yb 171 Rydberg States for High-Fidelity Two-Qubit Gates, *Phys. Rev. X* **15**, 011009 (2025).

[6] J. A. Muniz, M. Stone, D. T. Stack, M. Jaffe, J. M. Kindem, L. Wadleigh, E. Zalys-Geller, X. Zhang, C.-A. Chen, M. A. Norcia, J. Epstein, E. Halperin, F. Hummel, T. Wilkason, M. Li, K. Barnes, P. Battaglino, T. C. Bohdanowicz, G. Booth, A. Brown, M. O. Brown, W. B. Cairncross, K. Cassella, R. Coxe, D. Crow, M. Feldkamp, C. Griger, A. Heinz, A. M. W. Jones, H. Kim, J. King, K. Kotru, J. Lauigan, J. Marjanovic, E. Megidish, M. Meredith, M. McDonald, R. Morshead, S. Narayanaswami, C. Nishiguchi, T. Paule, K. A. Pawlak, K. L. Pudenz, D. R. Pérez, A. Ryou, J. Simon, A. Smull, M. Urbanek, R. J. M. Van De Veerdonk, Z. Vendeiro, T.-Y. Wu, X. Xie, and B. J. Bloom, High-Fidelity Universal Gates in the 171 Yb Ground-State Nuclear-Spin Qubit, *PRX Quantum* **6**, 020334 (2025).

[7] J. Beugnon, C. Tuchendler, H. Marion, A. Gaëtan, Y. Miroshnychenko, Y. R. P. Sortais, A. M. Lance, M. P. A. Jones, G. Messin, A. Browaeys, and P. Grangier, Two-dimensional transport and transfer of a single atomic qubit in optical tweezers, *Nature Phys* **3**, 696 (2007).

[8] D. Bluvstein, H. Levine, G. Semeghini, T. T. Wang, S. Ebadi, M. Kalinowski, A. Keesling, N. Maskara, H. Pichler, M. Greiner, V. Vuletić, and M. D. Lukin, A quantum processor based on coherent transport of entangled atom arrays, *Nature* **604**, 451 (2022).

[9] D. Bluvstein, S. J. Evered, A. A. Geim, S. H. Li, H. Zhou, T. Manovitz, S. Ebadi, M. Cain, M. Kalinowski, D. Hangleiter, J. P. Bonilla Ataides, N. Maskara, I. Cong, X. Gao, P. Sales Rodriguez, T. Karolyshyn, G. Semeghini, M. J. Gullans, M. Greiner, V. Vuletić, and M. D. Lukin, Logical quantum processor based on reconfigurable atom arrays, *Nature* **626**, 58 (2024).

[10] D. Bluvstein, A. A. Geim, S. H. Li, S. J. Evered, J. P. Bonilla Ataides, G. Baranes, A. Gu, T. Manovitz, M. Xu, M. Kalinowski, S. Majidy, C. Kokail, N. Maskara, E. C. Trapp, L. M. Stewart, S. Hollerith, H. Zhou, M. J. Gullans, S. F. Yelin, M. Greiner, V. Vuletić, M. Cain, and M. D. Lukin, A fault-tolerant neutral-atom architecture for universal quantum computation, *Nature* (2025).

[11] H. J. Manetsch, G. Nomura, E. Bataille, X. Lv, K. H. Leung, and M. Endres, A tweezer array with 6,100 highly coherent atomic qubits, *Nature* **647**, 60 (2025).

[12] F. Gyger, M. Ammenwerth, R. Tao, H. Timme, S. Snigirev, I. Bloch, and J. Zeiher, Continuous operation of large-scale atom arrays in optical lattices, *Phys. Rev. Res.* **6**, 033104 (2024).

[13] M. A. Norcia, H. Kim, W. B. Cairncross, M. Stone, A. Ryou, M. Jaffe, M. O. Brown, K. Barnes, P. Battaglino, T. C. Bohdanowicz, A. Brown, K. Cassella, C.-A. Chen, R. Coxe, D. Crow, J. Epstein, C. Griger, E. Halperin, F. Hummel, A. M. W. Jones, J. M. Kindem, J. King, K. Kotru, J. Lauigan, M. Li, M. Lu, E. Megidish, J. Marjanovic, M. McDonald, T. Mittiga, J. A. Muniz, S. Narayanaswami, C. Nishiguchi, T. Paule, K. A. Pawlak, L. S. Peng, K. L. Pudenz, D. Rodríguez Pérez, A. Smull, D. Stack, M. Urbanek, R. J. M. Van De Veerdonk, Z. Vendeiro, L. Wadleigh, T. Wilkason, T.-Y. Wu, X. Xie, E. Zalys-Geller, X. Zhang, and B. J. Bloom, Iterative Assembly of 171 Yb Atom Arrays with Cavity-Enhanced Optical Lattices, *PRX Quantum* **5**, 030316 (2024).

[14] N.-C. Chiu, E. C. Trapp, J. Guo, M. H. Abobeih, L. M. Stewart, S. Hollerith, P. L. Stroganov, M. Kalinowski, A. A. Geim, S. J. Evered, S. H. Li, X. Lyu, L. M. Peters, D. Bluvstein, T. T. Wang, M. Greiner, V. Vuletić, and M. D. Lukin, Continuous operation of a coherent 3,000-qubit system, *Nature* **646**, 1075 (2025).

[15] H. Zhou, C. Duckering, C. Zhao, D. Bluvstein, M. Cain, A. Kubica, S.-T. Wang, and M. D. Lukin, Resource Analysis of Low-Overhead Transversal Architectures for Reconfigurable Atom Arrays, in *Proceedings of the 52nd Annual International Symposium on Computer Architecture* (2025) pp. 1432–1448.

[16] J. Preskill, Reliable quantum computers, *Proceedings of the Royal Society of London. Series A: Mathematical, Physical and Engineering Sciences* **454**, 385 (1998).

[17] B. M. Terhal, Quantum error correction for quantum memories, *Rev. Mod. Phys.* **87**, 307 (2015).

[18] J. W. Lis, A. Senoo, W. F. McGrew, F. Rönchen, A. Jenkins, and A. M. Kaufman, Midcircuit Operations Using the omg Architecture in Neutral Atom Arrays, *Phys. Rev. X* **13**, 041035 (2023).

[19] M. A. Norcia, W. B. Cairncross, K. Barnes, P. Battaglino, A. Brown, M. O. Brown, K. Cassella, C.-A. Chen, R. Coxe, D. Crow, J. Epstein, C. Griger, A. M. W. Jones, H. Kim, J. M. Kindem, J. King, S. S. Kondov, K. Kotru, J. Lauigan, M. Li, M. Lu, E. Megidish, J. Marjanovic, M. McDonald, T. Mittiga, J. A. Muniz, S. Narayanaswami, C. Nishiguchi, R. Notermans, T. Paule, K. A. Pawlak, L. S. Peng, A. Ryou, A. Smull, D. Stack, M. Stone, A. Sucich, M. Urbanek, R. J. M. Van De Veerdonk, Z. Vendeiro, T. Wilkason, T.-Y. Wu, X. Xie, X. Zhang, and B. J. Bloom, Midcircuit Qubit Measurement and Rearrangement in a 171 Yb Atomic Array, *Phys. Rev. X* **13**, 041034 (2023).

[20] J. I. Cirac, A. K. Ekert, S. F. Huelga, and C. Macchiavello, Distributed quantum computation over noisy channels, *Phys. Rev. A* **59**, 4249 (1999).

[21] L. Jiang, J. M. Taylor, A. S. Sørensen, and M. D. Lukin, Distributed quantum computation based on small quantum registers, *Phys. Rev. A* **76**, 062323 (2007).

[22] N. H. Nickerson, Y. Li, and S. C. Benjamin, Topological quantum computing with a very noisy network and local error rates approaching one percent, *Nat. Commun.* **4**, 1756 (2013).

[23] N. H. Nickerson, J. F. Fitzsimons, and S. C. Benjamin, Freely Scalable Quantum Technologies Using Cells of 5-to-50 Qubits with Very Lossy and Noisy Photonic Links, *Phys. Rev. X* **4**, 041041 (2014).

[24] C. Monroe, R. Raussendorf, A. Ruthven, K. R. Brown, P. Maunz, L.-M. Duan, and J. Kim, Large-scale modular quantum-computer architecture with atomic memory and photonic interconnects, *Phys. Rev. A* **89**, 022317 (2014).

[25] J. P. Covey, H. Weinfurter, and H. Bernien, Quantum networks with neutral atom processing nodes, *npj Quantum Inf* **9**, 90 (2023).

[26] J. Ramette, J. Sinclair, N. P. Breuckmann, and V. Vuletić, Fault-tolerant connection of error-corrected qubits with noisy links, *npj Quantum Inf* **10**, 58 (2024).

[27] D. Main, P. Drmota, D. P. Nadlinger, E. M. Ainley, A. Agrawal, B. C. Nichol, R. Srinivas, G. Araneda, and D. M. Lucas, Distributed quantum computing across an optical network link, *Nature* **638**, 383 (2025).

[28] C. B. Young, A. Safari, P. Huft, J. Zhang, E. Oh, R. Chinnarasu, and M. Saffman, An architecture for quantum networking of neutral atom processors, *Appl. Phys. B* **128**, 151 (2022).

[29] J. Sinclair, J. Ramette, B. Grinkemeyer, D. Bluvstein, M. D. Lukin, and V. Vuletić, Fault-tolerant optical interconnects for neutral-atom arrays, *Phys. Rev. Research* **7**, 013313 (2025).

[30] E. M. Purcell, Proceedings of the American Physical Society: Spontaneous emission probabilities at radio frequencies, *Phys. Rev.* **69**, 674 (1946).

[31] J. Bochmann, M. Mücke, C. Guhl, S. Ritter, G. Rempe, and D. L. Moehring, Lossless State Detection of Single Neutral Atoms, *Phys. Rev. Lett.* **104**, 203601 (2010).

[32] R. Gehr, J. Volz, G. Dubois, T. Steinmetz, Y. Colombe, B. L. Lev, R. Long, J. Estève, and J. Reichel, Cavity-Based Single Atom Preparation and High-Fidelity Hyperfine State Readout, *Phys. Rev. Lett.* **104**, 203602 (2010).

[33] E. Deist, Y.-H. Lu, J. Ho, M. K. Pasha, J. Zeiher, Z. Yan, and D. M. Stamper-Kurn, Mid-Circuit Cavity Measurement in a Neutral Atom Array, *Phys. Rev. Lett.* **129**, 203602 (2022).

[34] B. Hu, J. Sinclair, E. Bytyqi, M. Chong, A. Rudelis, J. Ramette, Z. Vendeiro, and V. Vuletić, Site-Selective Cavity Readout and Classical Error Correction of a 5-Bit Atomic Register, *Phys. Rev. Lett.* **134**, 120801 (2025).

[35] B. Grinkemeyer, E. Guardado-Sánchez, I. Dimitrova, D. Shchepanovich, G. E. Mandopoulou, J. Borregaard, V. Vuletić, and M. D. Lukin, Error-detected quantum operations with neutral atoms mediated by an optical cavity, *Science* **387**, 1301 (2025).

[36] T. Wilk, S. C. Webster, A. Kuhn, and G. Rempe, Single-Atom Single-Photon Quantum Interface, *Science* **317**, 488 (2007).

[37] B. Weber, H. P. Specht, T. Müller, J. Bochmann, M. Mücke, D. L. Moehring, and G. Rempe, Photon-Photon Entanglement with a Single Trapped Atom, *Phys. Rev. Lett.* **102**, 030501 (2009).

[38] M. Lettner, M. Mücke, S. Riedl, C. Vo, C. Hahn, S. Baur, J. Bochmann, S. Ritter, S. Dürr, and G. Rempe, Remote Entanglement between a Single Atom and a Bose-Einstein Condensate, *Phys. Rev. Lett.* **106**, 210503 (2011).

[39] A. Reiserer, N. Kalb, G. Rempe, and S. Ritter, A quantum gate between a flying optical photon and a single trapped atom, *Nature* **508**, 237 (2014).

[40] A. Reiserer and G. Rempe, Cavity-based quantum networks with single atoms and optical photons, *Rev. Mod. Phys.* **87**, 1379 (2015).

[41] S. Ritter, C. Nölleke, C. Hahn, A. Reiserer, A. Neuzner, M. Uphoff, M. Mücke, E. Figueroa, J. Bochmann, and G. Rempe, An elementary quantum network of single atoms in optical cavities, *Nature* **484**, 195 (2012).

[42] C. Nölleke, A. Neuzner, A. Reiserer, C. Hahn, G. Rempe, and S. Ritter, Efficient Teleportation Between Remote Single-Atom Quantum Memories, *Phys. Rev. Lett.* **110**, 140403 (2013).

[43] S. Langenfeld, S. Welte, L. Hartung, S. Daiss, P. Thomas, O. Morin, E. Distante, and G. Rempe, Quantum Teleportation between Remote Qubit Memories with Only a Single Photon as a Resource, *Phys. Rev. Lett.* **126**, 130502 (2021).

[44] S. Daiss, S. Langenfeld, S. Welte, E. Distante, P. Thomas, L. Hartung, O. Morin, and G. Rempe, A quantum-logic gate between distant quantum-network modules, *Science* **371**, 614 (2021).

[45] A. Stute, B. Casabone, P. Schindler, T. Monz, P. O. Schmidt, B. Brandstätter, T. E. Northup, and R. Blatt, Tunable ion–photon entanglement in an optical cavity, *Nature* **485**, 482 (2012).

[46] V. Krutyanskiy, M. Meraner, J. Schupp, V. Krcmarsky, H. Hainzer, and B. P. Lanyon, Light-matter entanglement over 50 km of optical fibre, *npj Quantum Inf* **5**, 72 (2019).

[47] J. Schupp, V. Krcmarsky, V. Krutyanskiy, M. Meraner, T. Northup, and B. Lanyon, Interface between Trapped-Ion Qubits and Traveling Photons with Close-to-Optimal Efficiency, *PRX Quantum* **2**, 020331 (2021).

[48] P. Kobel, M. Breyer, and M. Köhl, Deterministic spin-photon entanglement from a trapped ion in a fiber Fabry–Perot cavity, *npj Quantum Inf* **7**, 6 (2021).

[49] V. Krutyanskiy, M. Galli, V. Krcmarsky, S. Baier, D. A. Fioretto, Y. Pu, A. Mazloom, P. Sekatski, M. Canteri, M. Teller, J. Schupp, J. Bate, M. Meraner, N. Sangouard, B. P. Lanyon, and T. E. Northup, Entanglement of Trapped-Ion Qubits Separated by 230 Meters, *Phys. Rev. Lett.* **130**, 050803 (2023).

[50] V. Krutyanskiy, M. Canteri, M. Meraner, J. Bate, V. Krcmarsky, J. Schupp, N. Sangouard, and B. P. Lanyon, Telecom-Wavelength Quantum Repeater Node Based on a Trapped-Ion Processor, *Phys. Rev. Lett.* **130**, 213601 (2023).

[51] V. Krutyanskiy, M. Canteri, M. Meraner, V. Krcmarsky, and B. Lanyon, Multimode Ion-Photon Entanglement over 101 Kilometers, *PRX Quantum* **5**, 020308 (2024).

[52] S. Gao, J. A. Blackmore, W. J. Hughes, T. H. Doherty, and J. F. Goodwin, Optimization of Scalable Ion-Cavity

Interfaces for Quantum Photonic Networks, *Phys. Rev. Applied* **19**, 014033 (2023).

[53] Y. Li and J. D. Thompson, High-Rate and High-Fidelity Modular Interconnects between Neutral Atom Quantum Processors, *PRX Quantum* **5**, 020363 (2024).

[54] S. G. Menon, N. Glachman, M. Pompili, A. Dibos, and H. Bernien, An integrated atom array-nanophotonic chip platform with background-free imaging, *Nat. Commun.* **15**, 6156 (2024).

[55] A. L. Shaw, A. Soper, D. Shadmany, A. Kumar, L. Palm, D.-Y. Koh, V. Kaxiras, L. Taneja, M. Jaffe, D. I. Schuster, and J. Simon, A cavity array microscope for parallel single-atom interfacing, [arXiv:2506.10919](https://arxiv.org/abs/2506.10919) (2025).

[56] H. Kübler, J. P. Shaffer, T. Baluktsian, R. Löw, and T. Pfau, Coherent excitation of Rydberg atoms in micrometre-sized atomic vapour cells, *Nat. Photonics* **4**, 112 (2010).

[57] W. Wang, D. Fomra, A. Agrawal, H. J. Lezec, and J. W. Britton, Can TCOs Transform Cavity-QED?, [arXiv:2506.02501](https://arxiv.org/abs/2506.02501) (2025).

[58] P. Horak, H. Ritsch, T. Fischer, P. Maunz, T. Puppe, P. W. H. Pinkse, and G. Rempe, Optical Kaleidoscope Using a Single Atom, *Phys. Rev. Lett.* **88**, 043601 (2002).

[59] T. Puppe, P. Maunz, T. Fischer, P. Pinkse, and G. Rempe, Single-Atom Trajectories in Higher-Order Transverse Modes of a High-Finesse Optical Cavity, *Physica Scripta* **T112**, 7 (2004).

[60] V. D. Vaidya, Y. Guo, R. M. Kroese, K. E. Ballantine, A. J. Kollár, J. Keeling, and B. L. Lev, Tunable-Range, Photon-Mediated Atomic Interactions in Multi-mode Cavity QED, *Phys. Rev. X* **8**, 011002 (2018).

[61] R. M. Kroese, B. P. Marsh, D. Atri Schuller, H. S. Hunt, A. N. Bourzutschky, M. Winer, S. Gopalakrishnan, J. Keeling, and B. L. Lev, Directly observing replica symmetry breaking in a vector quantum-optical spin glass, *Science* **389**, 1122 (2025).

[62] L. W. Clark, N. Schine, C. Baum, N. Jia, and J. Simon, Observation of Laughlin states made of light, *Nature* **582**, 41 (2020).

[63] R. M. Kroese, B. P. Marsh, K.-Y. Lin, J. Keeling, and B. L. Lev, High Cooperativity Using a Confocal-Cavity-QED Microscope, *PRX Quantum* **4**, 020326 (2023).

[64] A. E. Siegman, *Lasers* (University Science Books, 1986).

[65] A. P. Burgers, S. Ma, S. Saskin, J. Wilson, M. A. Alarcón, C. H. Greene, and J. D. Thompson, Controlling Rydberg Excitations Using Ion-Core Transitions in Alkaline-Earth Atom-Tweezer Arrays, *PRX Quantum* **3**, 020326 (2022).

[66] C. Baum, M. Jaffe, L. Palm, A. Kumar, and J. Simon, Optical mode conversion via spatiotemporally modulated atomic susceptibility, *Opt. Express* **31**, 528 (2023).

[67] G. Bornet, G. Emperaiger, C. Chen, F. Machado, S. Chern, L. Leclerc, B. Gély, Y. T. Chew, D. Barredo, T. Lahaye, N. Y. Yao, and A. Browaeys, Enhancing a Many-Body Dipolar Rydberg Tweezer Array with Arbitrary Local Controls, *Phys. Rev. Lett.* **132**, 263601 (2024).

[68] F. Orsi, N. Sauerwein, R. P. Bhatt, J. Faltinath, E. Fedotova, N. Reiter, T. Cantat-Moltrecht, and J.-P. Brantut, Cavity Microscope for Micrometer-Scale Control of Atom-Photon Interactions, *PRX Quantum* **5**, 040333 (2024).

[69] Z. Aqua and B. Dayan, Atom-Mediated Deterministic Generation and Stitching of Photonic Graph States, *PRX Quantum* **6**, 010340 (2025).

[70] J.-F. Morizur, L. Nicholls, P. Jian, S. Armstrong, N. Treps, B. Hage, M. Hsu, W. Bowen, J. Janousek, and H.-A. Bachor, Programmable unitary spatial mode manipulation, *JOSA A* **27**, 2524 (2010).

[71] N. K. Fontaine, R. Ryf, H. Chen, D. T. Neilson, K. Kim, and J. Carpenter, Laguerre-Gaussian mode sorter, *Nat. Commun.* **10**, 1865 (2019).

[72] N. K. Fontaine, H. Chen, M. Mazur, L. Dallachiesa, K. Kim, R. Ryf, D. Neilson, and J. Carpenter, Hermite-Gaussian mode multiplexer supporting 1035 modes, in *Optical Fiber Communication Conference (OFC) 2021* (Optica Publishing Group, Washington, DC, 2021) p. M3D.4.

[73] Y. Zhang and N. K. Fontaine, Multi-Plane Light Conversion: A Practical Tutorial, [arXiv:2304.11323](https://arxiv.org/abs/2304.11323) (2023).

[74] M. Choi, C. Pluchar, W. He, S. Guha, and D. Wilson, Quantum limited imaging of a nanomechanical resonator with a spatial mode sorter, [arXiv:2411.04980](https://arxiv.org/abs/2411.04980) (2024).

[75] M. Shirasaki, Large angular dispersion by a virtually imaged phased array and its application to a wavelength demultiplexer, *Opt. Lett.* **21**, 366 (1996).

[76] S. Xiao, A. M. Weiner, and C. Lin, A dispersion law for virtually-imaged phased-array spectral dispersers based on paraxial-wave theory, in *Conference on Lasers and Electro-Optics/International Quantum Electronics Conference and Photonic Applications Systems Technologies (2004)*, Paper CThCC5 (Optica Publishing Group, 2004) p. CThCC5.

[77] B. S. Leonov, A. A. Rad, Y. Wu, and C. M. Limbach, Application of a pulsed OPO seeded by a CW OPO to investigation of linewidth effects on TALIF excitation efficiency, *Optics & Laser Technology* **144**, 107370 (2021).

[78] A. D. Boozer, A. Boca, R. Miller, T. E. Northup, and H. J. Kimble, Cooling to the Ground State of Axial Motion for One Atom Strongly Coupled to an Optical Cavity, *Phys. Rev. Lett.* **97**, 083602 (2006).

[79] C. Knoernschild, X. L. Zhang, L. Isenhower, A. T. Gill, F. P. Lu, M. Saffman, and J. Kim, Independent individual addressing of multiple neutral atom qubits with a micromirror-based beam steering system, *Appl. Phys. Lett.* **97**, 134101 (2010).

[80] T. M. Graham, E. Oh, and M. Saffman, Multiscale architecture for fast optical addressing and control of large-scale qubit arrays, *Appl. Opt.* **62**, 3242 (2023).

[81] A. J. Menssen, A. Hermans, I. Christen, T. Propson, C. Li, A. J. Leenheer, M. Zimmermann, M. Dong, H. Larocque, H. Raniwala, G. Gilbert, M. Eichenfield, and D. R. Englund, Scalable photonic integrated circuits for high-fidelity light control, *Optica* **10**, 1366 (2023).

[82] B. Zhang, P. Peng, A. Paul, and J. D. Thompson, Scaled local gate controller for optically addressed qubits, *Optica* **11**, 227 (2024).

[83] I. Christen, T. Propson, M. Sutula, H. Sattari, G. Choong, C. Panuski, A. Melville, J. Mallek, C. Brabec, S. Hamilton, P. B. Dixon, A. J. Menssen, D. Braje, A. H. Ghadimi, and D. Englund, An integrated photonic engine for programmable atomic control, *Nat Commun* **16**, 82 (2025).

[84] Q. Lin, S. Fang, Y. Yu, Z. Xi, L. Shao, B. Li, and

M. Li, Optical multi-beam steering and communication using integrated acousto-optics arrays, *Nat. Commun.* **16**, 4501 (2025).

[85] M. Zhao, M. Singh, A. Singh, H. Thoreen, R. J. DeAngelo, D. Dominguez, A. Leenheer, F. Peyskens, A. Lukin, D. Englund, M. Eichenfield, N. Gemelke, and N. H. Wan, An integrated photonics platform for high-speed, ultrahigh-extinction, many-channel quantum control, [arXiv:2508.09920](https://arxiv.org/abs/2508.09920) (2025).

[86] A. G. Fowler, M. Mariantoni, J. M. Martinis, and A. N. Cleland, Surface codes: Towards practical large-scale quantum computation, *Phys. Rev. A* **86**, 032324 (2012).

[87] J. O’Gorman and E. T. Campbell, Quantum computation with realistic magic-state factories, *Phys. Rev. A* **95**, 032338 (2017).

[88] C. Gidney and M. Ekerå, How to factor 2048 bit RSA integers in 8 hours using 20 million noisy qubits, *Quantum* **5**, 433 (2021).

[89] C. Gidney, How to factor 2048 bit RSA integers with less than a million noisy qubits, [arXiv:2505.15917](https://arxiv.org/abs/2505.15917) (2025).

[90] P. Maunz, S. Olmschenk, D. Hayes, D. N. Matsukevich, L.-M. Duan, and C. Monroe, Heralded Quantum Gate between Remote Quantum Memories, *Phys. Rev. Lett.* **102**, 250502 (2009).

[91] D. Gottesman and I. L. Chuang, Demonstrating the viability of universal quantum computation using teleportation and single-qubit operations, *Nature* **402**, 390 (1999).

[92] T. van Leent, M. Bock, F. Fertig, R. Garthoff, S. Eppelt, Y. Zhou, P. Malik, M. Seubert, T. Bauer, W. Rosenfeld, W. Zhang, C. Becher, and H. Weinfurter, Entangling single atoms over 33 km telecom fibre, *Nature* **607**, 69 (2022).

[93] S. Singh, F. Gu, S. de Bone, E. Villaseñor, D. Elkouss, and J. Borregaard, Modular Architectures and Entanglement Schemes for Error-Corrected Distributed Quantum Computation, [arXiv:2408.02837](https://arxiv.org/abs/2408.02837) (2024).

[94] J. Hofmann, M. Krug, N. Ortegel, L. Gérard, M. Weber, W. Rosenfeld, and H. Weinfurter, Heralded Entanglement Between Widely Separated Atoms, *Science* **337**, 72 (2012).

[95] W. Rosenfeld, D. Burchardt, R. Garthoff, K. Redeker, N. Ortegel, M. Rau, and H. Weinfurter, Event-Ready Bell Test Using Entangled Atoms Simultaneously Closing Detection and Locality Loopholes, *Phys. Rev. Lett.* **119**, 010402 (2017).

[96] L. J. Stephenson, D. P. Nadlinger, B. C. Nichol, S. An, P. Drmota, T. G. Ballance, K. Thirumalai, J. F. Goodwin, D. M. Lucas, and C. J. Ballance, High-Rate, High-Fidelity Entanglement of Qubits Across an Elementary Quantum Network, *Phys. Rev. Lett.* **124**, 110501 (2020).

[97] J. O’Reilly, G. Toh, I. Goetting, S. Saha, M. Shalaev, A. L. Carter, A. Risinger, A. Kalakuntla, T. Li, A. Verma, and C. Monroe, Fast Photon-Mediated Entanglement of Continuously Cooled Trapped Ions for Quantum Networking, *Phys. Rev. Lett.* **133**, 090802 (2024).

[98] P. Thomas, L. Ruscio, O. Morin, and G. Rempe, Efficient generation of entangled multiphoton graph states from a single atom, *Nature* **608**, 677 (2022).

[99] O. Morin, M. Körber, S. Langenfeld, and G. Rempe, Deterministic Shaping and Reshaping of Single-Photon Temporal Wave Functions, *Phys. Rev. Lett.* **123**, 133602 (2019).

[100] N. Berthelsen, S. J. S. Tan, E. Huang, and D. Gottesman, Adaptive Syndrome Extraction, *PRX Quantum* **6**, 030307 (2025).

[101] A. N. Utama, C. H. Chow, C. H. Nguyen, and C. Kurtseifer, Coupling light to higher order transverse modes of a near-concentric optical cavity, *Opt. Express* **29**, 8130 (2021).